Available online at www.sciencedirect.com
ScienceDirect
International Journal of Multiphase Flow 32 (2006) 957–971
International Journal of Multiphase Flow
www.elsevier.com/locate/ijmulflow

Measurements and high-speed visualizations of flow boiling of a dielectric fluid in a silicon microchannel heat sink

Tailian Chen, Suresh V. Garimella *

Cooling Technologies Research Center, School of Mechanical Engineering, 585 Purdue Mall, Purdue University, West Lafayette, IN 47907-2088, USA

Received 22 February 2006; received in revised form 8 March 2006

Abstract

Experiments were conducted to investigate flow boiling heat transfer to a dielectric fluid in a silicon chip-integrated microchannel heat sink. Twenty-four microchannels, each 389 μm × 389 μm in cross-section, were fabricated into the 12.7 mm × 12.7 mm silicon substrate. High-speed visualizations (at 12,500 frames per second) were performed simultaneously with heat transfer and pressure drop measurements to investigate the physics of flow boiling in parallel microchannel arrays. At low heat fluxes, bubbly flow is dominant, with the bubbles coalescing to form vapor slugs as the heat flux is increased. At high heat fluxes, the flow regimes in the downstream portion of the microchannels are characteristic of alternating wispy-annular flow and churn flow, while flow reversal is observed in the upstream region near the microchannel inlet. Local heat transfer measurements, obtained at three flow rates ranging from 35 to 60 ml/min, show that at lower heat fluxes, the heat transfer coefficient increases with increasing heat flux. The heat transfer coefficient in fully developed boiling is seen to be independent of flow rate in this range. At higher heat fluxes (exceeding 542, 673, 730 kW/m^2, respectively, for flow rates of 35, 47 and 60 ml/min), this trend is reversed, and the heat transfer coefficient decreases with further increases in heat flux due to partial dryout in some of the microchannels. Heat fluxes at which fully developed boiling is achieved depend on the flow rate. The pressure drop in fully developed boiling increases with increasing heat flux and is independent of flow rate for the test conditions considered in this work.

Keywords: Flow boiling; Microchannels; Visualization; Flow patterns; Flow reversal; Electronics cooling

1. Introduction

Two-phase convective heat transfer in microchannels is attractive in view of the high heat transfer coefficients and reduced non-uniformity of the wall temperature that can be achieved. Flow boiling in tubes or channels of hydraulic diameters on the order of 1 mm and less has been shown to be significantly different

* Corresponding author. Tel.: +1 765 494 5621; fax: +1 765 494 0539.
E-mail address: sureshg@purdue.edu (S.V. Garimella).

0301-9322/$ - see front matter © 2006 Elsevier Ltd. All rights reserved.
doi:10.1016/j.ijmultiphaseflow.2006.03.002

from that in larger channels (Lazarek and Black, 1982; Thome, 2004). For flow boiling in larger channels, both convective and nucleate boiling heat transfer are considered important and overall heat transfer has typically been treated by combining these two components. However, since flow in microchannels is usually laminar, conventional boiling correlations were found to over-predict the boiling heat transfer (Liu and Garimella, 2005); correlations based on nucleate boiling, on the other hand, gave better predictions for flow boiling in microchannels (Kew and Cornwell, 1997).

Results obtained in a study of flow boiling of R-134a in tubes of three different diameters (0.5, 1.1, 3.1 mm) by Saitoh et al. (2005) showed that the contribution of forced convective heat transfer to the overall heat transfer decreases with decreasing tube diameter. Based on space confinement effects of bubbles within a channel, Kew and Cornwell (1997) proposed a threshold hydraulic diameter, $D_h = (4\sigma/g(\rho_l - \rho_v))^{0.5}$, in which σ is liquid surface tension, g is the gravitational acceleration, and ρ_l and ρ_v are liquid and vapor densities. For diameters smaller than this threshold value, conventional methods were said to be unsuitable in predicting both the heat transfer rates and flow pattern transitions. Furthermore, Peng et al. (1998) and Lin et al. (1994) proposed that bubble nucleation can be inhibited in channels of hydraulic diameters less than a critical value. Huo et al. (2004) studied flow boiling of R-134a in stainless steel tubes of diameters 4.3 mm and 2 mm. Their results showed that at low vapor qualities (0.4–0.5 for the 4.3 mm tube, 0.2–0.3 for the 2 mm tube) nucleate boiling heat transfer dominates. At higher vapor qualities, the heat transfer coefficient decreased with increasing vapor quality. Visualizations revealed six flow patterns: dispersed bubble, bubbly flow, slug flow, churn flow, annular flow, and mist flow. It was also shown that for smaller tubes, specific two-phase flow patterns are realized at lower heat fluxes relative to the heat fluxes at which the corresponding patterns are seen for larger tubes. In a study of air–water two-phase flow patterns under adiabatic conditions by Coleman and Garimella (1999), both channel diameter and surface tension were shown to play an important role in determining flow patterns and their transitions in smaller diameter tubes. They found that a decrease in tube diameter led to a higher value of superficial liquid velocity needed for the transition from slug flow to a dispersed flow regime.

Flow boiling heat transfer has been most commonly analyzed using a separated flow model or a homogeneous flow model. While it is understood that flow-pattern based models would be more accurate for predicting heat transfer in flow boiling, progress in this direction has been limited owing to the lack of understanding of the complex phenomena involved in flow boiling in microchannels. The occurrence of flow instabilities is common in flow boiling in microchannels, further complicating modeling efforts. Kandlikar (2002) reported that three flow patterns – isolated bubbles, confined bubbles or bubble slugs, and annular flow – are commonly encountered during flow boiling in small channels of hydraulic diameter on the order of 1 mm. However, more complicated flow patterns attributed to flow instabilities have also been reported. In an experimental study of flow boiling of water in both a single channel and six parallel minichannels of hydraulic diameter 1 mm, Kandlikar et al. (2001) found that annular flow occurs only as an intermittent condition after the growth of a vapor slug. Hetsroni et al. (2001) observed periodic annular flow represented by a symmetrically distributed liquid ring surrounding the vapor core interspersed with periodic dry zones characterized by the occurrence of dry spots on the channel walls. Visualization results obtained by Xu et al. (2005) showed that the flow patterns in all microchannels repeat themselves over a cycle timescale of milliseconds, consisting of liquid refilling, bubble nucleation and coalescence, and transient annular flow. Wu and Cheng (2003) observed that two-phase and single-phase flows appear alternatively with time in microchannels, leading to fluctuations in wall temperature, pressure drop, and mass flux. The fluctuations in wall temperature and pressure drop due to flow instabilities have also been measured by other investigators (Hetsroni et al., 2002; Brutin and Tadrist, 2003; Wu and Cheng, 2004).

In the present work, high-speed visualizations covering a range of vapor qualities with simultaneous heat transfer and pressure drop measurements are performed in a unique test vehicle to investigate flow boiling in a parallel array of microchannels. The test vehicle allows individual control of imposed heat flux over 25 elements of the heated surface; highly localized temperature measurements can also be obtained at 25 locations on the test substrate. The flow patterns and their transitions that have been visualized are expected to serve as the foundation for developing flow-pattern based models. In addition, the highly transient flow reversal phenomena captured in the visualizations provide important insights into flow boiling in microchannels.

2. Experiments

2.1. Test loop

A schematic diagram of the test loop designed and used for the experiments is shown in Fig. 1. A magnetically coupled gear pump drives the coolant through the closed loop while a precision flow meter (McMillan Company, model S-114) monitors the flow rate. A preheater installed upstream of the test section controls the degree of inlet subcooling and a heat exchanger positioned after the test section cools down the fluid. The coolant, a perfluorinated dielectric liquid, FC-77, picks up heat in the microchannel test section which is discussed in the next section. The liquid is fully degassed before initiating the tests. The two degassing ports shown in Fig. 1 are used to degas the liquid in the reservoir and evacuate air from the test loop. Details of the degassing scheme and procedures are available in Chen and Garimella (2005, in press). Fully degassed FC-77 has a boiling point 97 °C at one atmospheric pressure. Tests are conducted at three flow rates, 35, 47, and 60 ml/min, with the liquid inlet temperature held at 71 ± 1.0 °C. The corresponding Reynolds numbers are 169, 226, and 289, respectively. Other relevant properties of FC-77 at 71 °C (liquid temperature at the inlet manifold) are provided in Table 1. The pressure in the outlet manifold of the test section is maintained at one atmosphere. The pressure drop across the microchannel array is measured using a differential pressure transducer.

A high-speed imaging system (with a Photron FASTCAM-Ultima APX CMOS camera) is used to visualize two-phase flow patterns at the rate of 12,500 frames per second at a 512×256 resolution. Heat transfer and pressure drop measurements are obtained using a computer-based data acquisition system when the boiling process in the microchannels reaches a steady state at each heat flux.

2.2. Test vehicle

The test vehicle, shown in Fig. 2(a), consists of a silicon thermal test chip mounted on a print circuit board (PCB) with flip-chip technology. The 12.7 mm × 12.7 mm test chip incorporates 25 individual heating elements

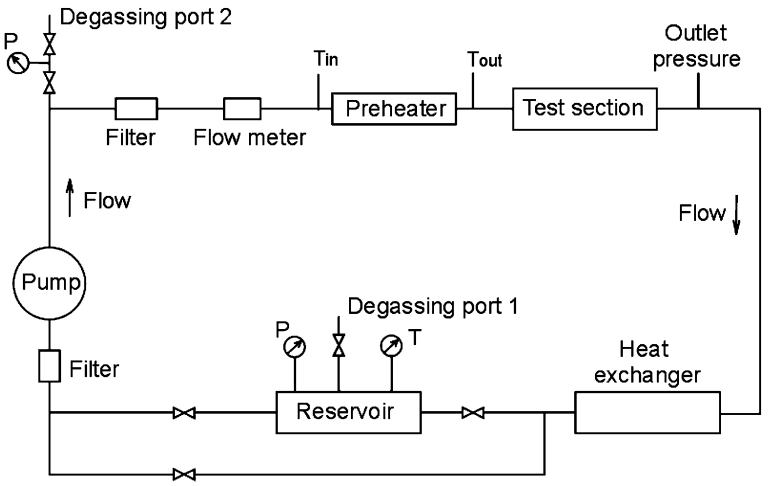

Fig. 1. Experimental test loop.

Table 1
Properties of boiling fluid (FC-77) at 71 °C (3M Corporation, 1995)

Prandtl number	Dynamic viscosity (kg/m s)	Density (kg/m^3)	Thermal conductivity (W/m K)	Heat capacity (J/kg K)	Critical pressure (MPa)	Molecular weight
11.7	6.17×10^{-4}	1664	0.059	1124	1.58	314

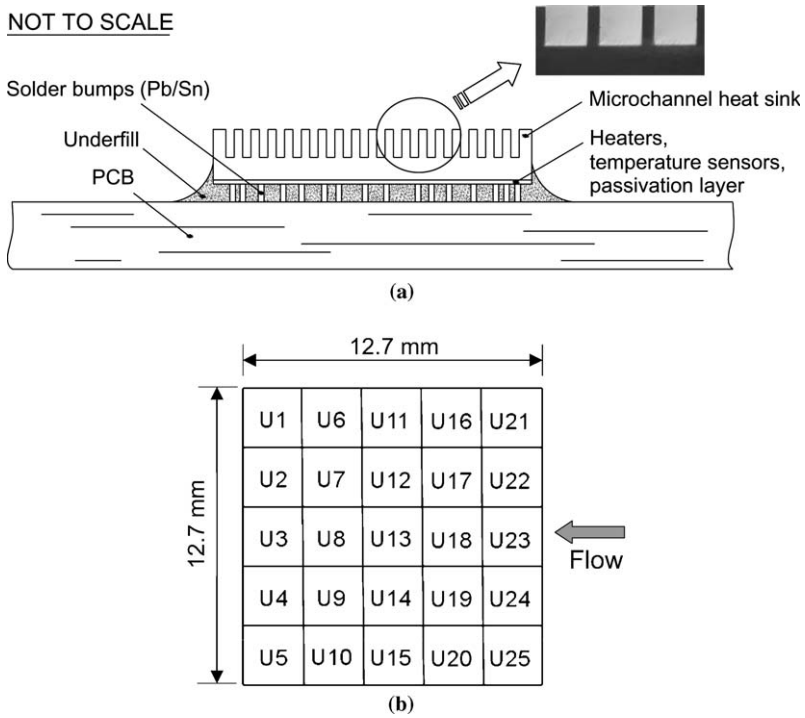

Fig. 2. (a) Cross-section showing fabrication details of the test vehicle, and (b) the arrangement of the 25 heating elements (not shown in the figure are 25 temperature sensors, each located at the center of a heating element).

(doped silicon wells), each of approximate size 2.54 mm × 2.54 mm. A temperature sensor (consisting of five p–n junction diodes in series) is located at the center of each heating element. Each heating element has a resistance of $28.4 \pm 0.2\ \Omega$ at room temperature. In the tests for the present work, a uniform heat flux is desired on the test substrate. Therefore, the 25 heating elements are connected in parallel and supplied with a single DC voltage source. The heat generated by each element is calculated from the applied voltage and the calibrated resistance. The arrangement of the 25 heating elements (U1–U25) on the thermal test chip is shown in Fig. 2(b). Visualizations reported here are obtained in the microchannels near the centerline of the test substrate in the exit region. The corresponding local heat transfer coefficients are based on measurements from the U3 temperature sensor.

The microchannels are machined into the backside of the silicon thermal test chip (opposite side from the heating elements and temperature sensors) by saw cutting. Twenty-four microchannels, each with a square cross-section of 389 μm × 389 μm are accommodated on the test chip in this manner. The width of the fins between the microchannels is 100 μm. A photograph showing the profile of the microchannels from one end is shown as an inset in Fig. 2(a).

For a given current (approximately 100 μA) passing through a diode, the voltage drop across the diode depends only on the temperature, with a dependence of approximately −2 mV/°C. The exact voltage–temperature relationship for each diode is obtained by calibration; the resistances of the 25 heating elements as a function of temperature are also measured during this process. The calibration is done by placing the test vehicle in a controlled, uniform-temperature oven. Five thermocouples positioned at five different locations on the test vehicle monitor its temperature. Measurements from all five thermocouples are the same and remain unchanged with time; therefore, the diodes are also expected to be at this same temperature. When this condition is reached, the voltages from the 25 temperature sensors and the resistances of the 25 heating elements are recorded. This calibration shows that all sensors have a temperature dependence that is well represented by $V = -0.0104\ T_b\ (°C) + 3.482$. During boiling experiments, this relationship is used to determine the temperature, T_b, from the measured voltage drop across each temperature sensor. The resistance of each heating

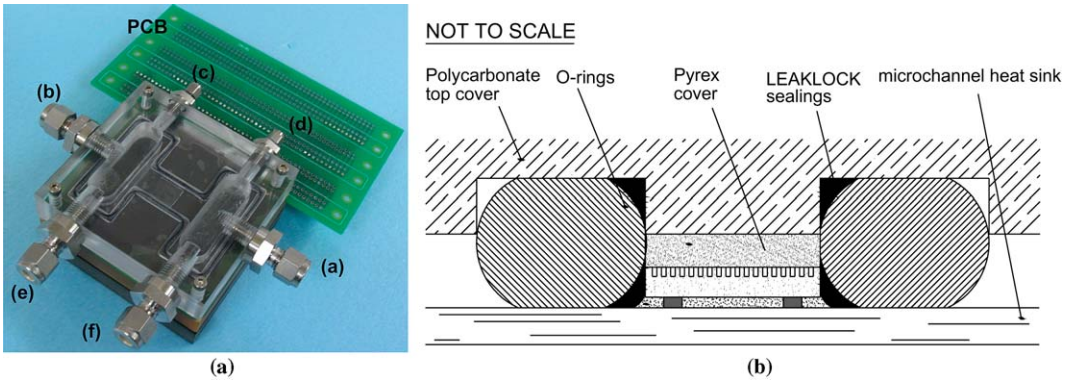

Fig. 3. (a) Photograph of assembled test section ('a' and 'b' are fluid inlet and outlet, 'c' and 'd' are thermocouple insertion ports, and 'e' and 'f' are connected to the differential pressure transducer), and (b) cut-away view perpendicular to the microchannels showing the assembly details (flow is into the page in this view).

element is observed to increase almost linearly with temperature, at a rate of approximately 2 Ω for a temperature increase of 100 °C. The resistance variation with temperature is taken into account in calculating the heat generation by the heating elements.

2.3. Test section assembly

Fig. 3(a) shows a photograph of the assembled test section, including the printed circuit board holding the test chip, polycarbonate flow containment, and ports for fluid inlet/outlet, thermocouples and pressure transducer. The test vehicle is sandwiched between the top cover and bottom support. Thermocouples inserted through ports 'c' and 'd' in the figure measure the temperatures in the inlet and outlet manifolds, respectively. Differential pressure is measured using ports 'e' and 'f'. An additional print circuit board, attached to the test section, is used as an extension board for electrical access to the heaters and temperature sensors on the test vehicle. Fig. 3(b) provides assembly details (the bottom support is not included). The microchannel heat sink has a 0.6 mm thick Pyrex lid (melting point >400 °C) that is held in place by a top cover integral to the test section assembly. The top cover is machined from polycarbonate and contains O-ring grooves as shown. LEAKLOCK sealing fills the corners of the O-ring grooves to prevent liquid bypass from inlet to outlet. The absence of a liquid bypass path is verified by comparing the pressure drop in single phase flow through the microchannels against expected values, prior to the commencement of two-phase flow experiments.

3. Data reduction and uncertainty analysis

An energy balance can be written *for each heating element* as

$$\dot{q}_{\text{total}} = \dot{q}_{\text{fluid}} + \dot{q}_{\text{loss}}, \tag{1}$$

in which the total heat generation $\dot{q}_{\text{total}}$ is obtained directly as $\dot{q}_{\text{total}} = V^2/R$ from the applied voltage, V, and the heating element resistance, R, $\dot{q}_{\text{fluid}}$ is the heat transfer rate from the heating element to the fluid in the microchannels, and $\dot{q}_{\text{loss}}$ is the heat loss determined experimentally by measuring the heat input that can be sustained at each heat sink base temperature before the test assembly is charged with coolant. A relationship is thus obtained between the heat loss and the heat sink base temperature T_{b} for each heating element. For example, the heat loss for heating element U3 (shown in Fig. 2(b)) is represented by $\dot{q}_{\text{loss}} = 0.1229 \times T_{\text{b}} - 2.7821$ from the measured heat losses. The linear increase in heat loss with temperature indicates that the losses are primarily by conduction from the test section to the ambient. This heat loss-temperature relationship is used in Eq. (1) to determine the heat transfer to the fluid, $\dot{q}_{\text{fluid}}$, during the boiling experiments. *Local* heat transfer coefficients, h, were calculated using

$$h = \frac{\dot{q}_{\text{fluid}}}{(T_w - T_{\text{sat}})A}. \tag{2}$$

In Eq. (2), h is obtained based on the heating element area, A (0.0645 cm^2, which is 1/25th of the total heat sink base area). The heat fluxes, q'', reported in this work are also based on the heating element area, i.e., $q'' = \dot{q}_{\text{fluid}}/A$. It should be noted that due to the pressure drop in microchannels, the local saturation temperature T_{sat} in Eq. (2) decreases in the flow direction. A linear pressure drop from the inlet to the exit of the microchannels is assumed to obtain the local pressure in the microchannels, and thus the local saturation temperature, T_{sat}. The wall temperature T_w in Eq. (2) is obtained by correcting the temperature measured at the bottom of the microchannel substrate T_b using

$$T_w = T_b - \frac{\dot{q}_{\text{fluid}} t_b}{kA}, \tag{3}$$

in which t_b is the distance from the heat sink base to the bottom of the microchannel, and k is the thermal conductivity of the silicon substrate.

Uncertainties in the measured quantities presented in this work include ±3.3% to 5.7% in flow rate over the range considered, and 0.9–11.4% in the pressure drop measurements for measured values in the range of 300–3500 Pa; the larger uncertainties occur at smaller measured values. The wall temperature uncertainty comes from calibration of the temperature sensors and from correction for the temperature drop from the heat sink base as in Eq. (3). Wall temperature uncertainty due to calibration is estimated to be ±0.2 °C. Since the temperature correction for the temperature drop across the thin silicon substrate (0.14–0.57 °C for the heat fluxes tested) is much smaller than T_b, its contribution to the wall temperature uncertainty is neglected. Uncertainties in the heat transfer coefficient arise from those in the determination of heat transfer rate into the microchannels and the wall temperature measurements. Following a standard approach (Kline and McClintock, 1953), the uncertainty in heat transfer coefficient is estimated to be in the range of 1.8–17%, with the larger uncertainties occurring at the lower heat fluxes.

4. Results and discussion

Visualizations have been performed at a flow rate of 47 ml/min over a wide range of heat fluxes corresponding to a maximum thermodynamic vapor quality of 0.63 at the exit of the microchannels. At each heat flux, heat transfer and pressure drop were measured simultaneously as the visualizations were conducted. A cool light (from Kenka–Sass–Wolf) is used for illumination during the visualizations. In order to check whether illumination source leads to additional heat input by radiation to the fluid, heat transfer and pressure drop measurements were made under identical conditions with and without the illumination being provided. Fig. 4 shows that the measured wall temperatures and pressure drops for the cases with and without illumination are in good agreement, demonstrating that the illumination source does not have a thermal impact on the experimental measurements.

The different flow patterns visualized in the experiments are discussed in the rest of this section.

4.1. Bubbly and slug flows

The wall temperature, heat transfer coefficient, and pressure drop measured during the visualizations at a flow rate of 47 ml/min are shown in Fig. 5 as functions of both heat flux and the exit thermodynamic vapor quality, x_e, which is calculated from an energy balance:

$$x_e = \frac{1}{h_{fg}}\left[\frac{\dot{q}_{\text{fluid}}}{\rho Q} - C_p(T_{\text{sat}} - T_{\text{in}})\right]. \tag{4}$$

In Eq. (4), h_{fg} is the latent heat, Q the flow rate, and C_p the specific heat of the coolant fluid. As seen in Fig. 5(a), the heat flux of 269 kW/m^2 marks the point beyond which the temperature-heat flux slope moderates significantly, with an associated increase in the slope of the heat transfer coefficient curve. Fig. 5(b) also shows an approximately linear increase in pressure drop with increasing heat flux beyond this value of heat flux. As

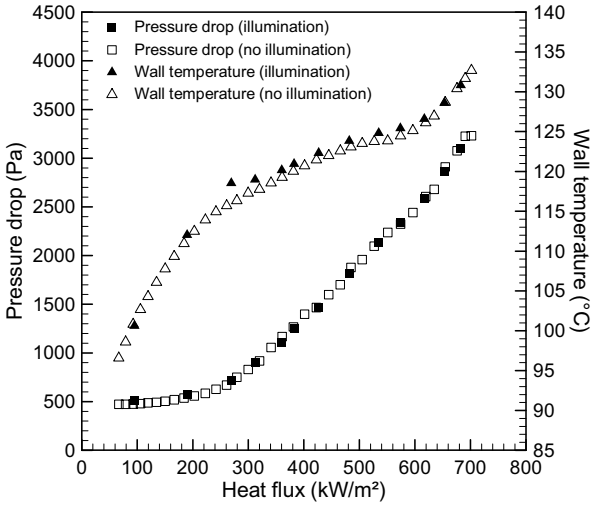

Fig. 4. Wall temperature and pressure drop measurements with and without the illumination source powered up.

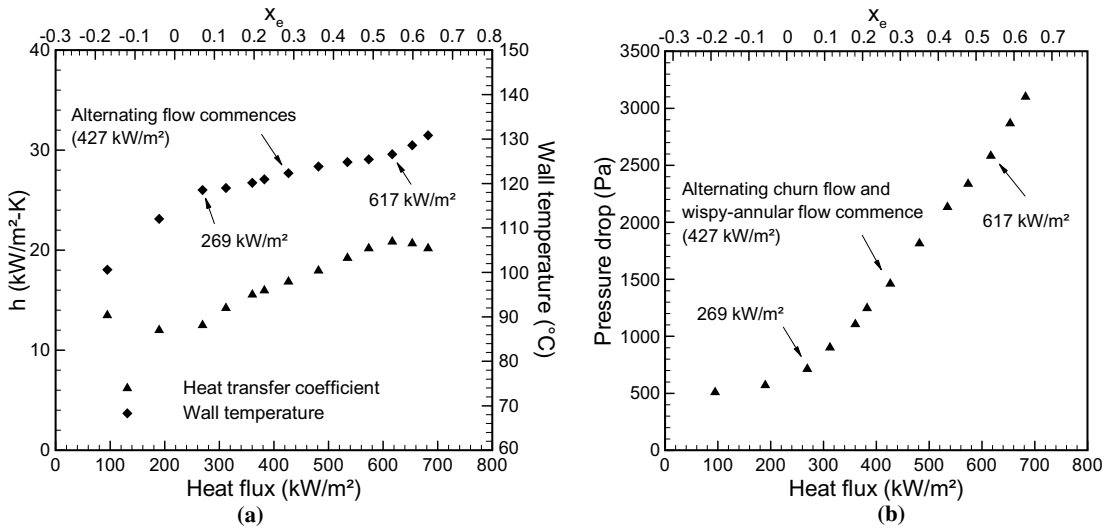

Fig. 5. Measurements of (a) heat transfer coefficient and wall temperature, and (b) pressure drop, as functions of heat flux and the exit vapor quality.

will be discussed further in the next section, the heat flux of 427 kW/m^2 is the point at which flow reversal starts to occur near the microchannel inlet, leading to alternating flow patterns of churn and wispy-annular flows in the downstream regions. The heat flux of 617 kW/m^2 is the demarcation point beyond which the heat transfer coefficient begins to decrease with further increases in heat flux.

Typical images from the visualizations obtained at the six lowest heat fluxes considered in Fig. 5 are shown in Fig. 6. At heat fluxes of 94 and 189 kW/m^2, bubbles are observed to nucleate on the channel walls. As the bubbles grow to a certain size, they detach and move downstream. These bubbles are rarely observed to coalesce, and are also largely confined to the vicinity of the channel walls. At the heat fluxes 269 and 312 kW/m^2, both nucleation density and bubble growth rate are much increased, leading to strong bubble interactions and frequent merging of bubbles. Bubbles were observed to grow well into the bulk of the channel; some bubbles are of a size to almost span the entire microchannel width. Based on these visualizations, it is noted in this work that at heat fluxes of 269 kW/m^2 and higher, the boiling process enters a fully developed regime; at lower fluxes, a

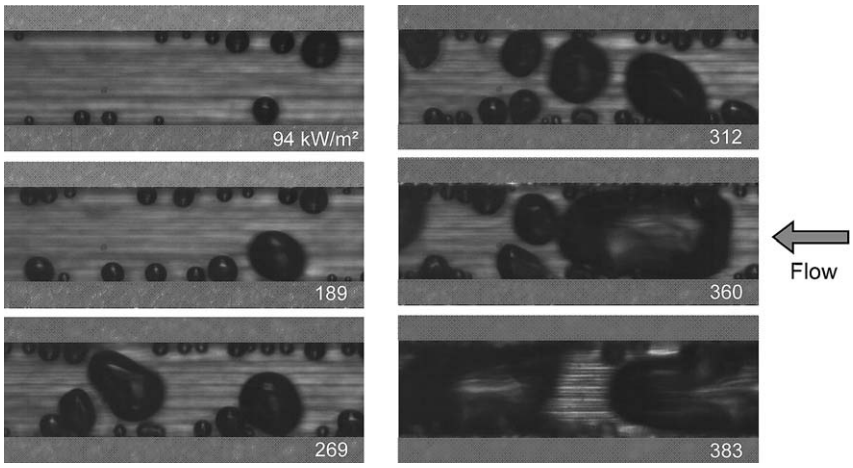

Fig. 6. Visualizations of boiling processes at low heat fluxes.

partial boiling regime is realized. In fact, it is seen in Fig. 5 that the vapor quality at the heat flux of 269 kW/m^2 is slightly above zero (0.054). It appears that a transition from partial to fully developed boiling is the physical mechanism for the observed changes in slopes at the heat flux of 269 kW/m^2 in Fig. 5.

The flow pattern at a heat flux of 360 kW/m^2 in Fig. 6 shows that vapor slugs are formed in the microchannels as a result of the merging of upstream bubbles. In between the passing of vapor slugs, bubbles are observed to nucleate and grow violently at the walls. As the vapor slugs travel downstream, these new bubbles nucleated on the walls are subsumed into the vapor slugs, contributing to an elongation of the slugs. The flow pattern at a heat flux of 383 kW/m^2 in the figure shows these elongated vapor slugs.[1]

4.2. Alternating churn flow and wispy-annular flow

A sustained slug flow pattern as seen in Fig. 6 at the heat flux of 360 and 383 kW/m^2 is realized over only a narrow range of heat flux. As the heat flux is increased to 427 kW/m^2, the flow pattern becomes intermittent, alternating between a churn flow and a wispy-annular flow pattern. The wispy-annular flow follows the churn flow, and the two patterns repeat in this alternating manner; Fig. 7 shows the commencement of churn flow following the wispy-annular flow at a heat flux of 427 kW/m^2. Fig. 8 shows images of typical churn flow and wispy-annular flow captured 5.84 ms after and 8.72 ms prior to the commencement of the churn flow shown in Fig. 7, respectively. The times of +5.84 ms and −8.72 ms in Fig. 8 are referenced with respect to the time when churn flow commences at the instant shown in Fig. 7. Schematic sketches of the observed flow patterns are included in both Figs. 7 and 8. As will be seen later in this discussion, the alternating flow patterns result from flow reversal upstream in the microchannels. This alternating flow regime pattern continues as the heat flux is increased further, until complete dryout of the channel walls is observed.

In churn flow, the typical flow pattern is dispersed bubbles or vapor chunks flowing with the bulk liquid. Unlike the bubbly flow at low heat fluxes, bubbles or vapor chunks in churn flow are swept from upstream and distributed over the entire channel cross-section. Wispy-annular flow is characterized by dispersed thin liquid films on the channel walls and a vapor core in the rest of the channel cross-section. Churn flow was observed to last for approximately 20 ms at the heat flux 427 kW/m^2 before developing into wispy-annular flow, which lasted for approximately 15 ms before churn flow resumed. Thus, the period of the alternating flow at the heat flux 427 kW/m^2 is approximately 35 ms (frequency $\approx$ 30 Hz). Cross-sections are sketched in Fig. 9 based on the observed flow patterns at various depths of focus in the microchannel. It is obvious that the void fraction, and thus the vapor quality, during wispy-annular flow is much larger than that in churn flow.

[1] To assist with interpretation of the still images included here, short movie clips from the visualizations are provided at www.ecn.purdue.edu/ECL.

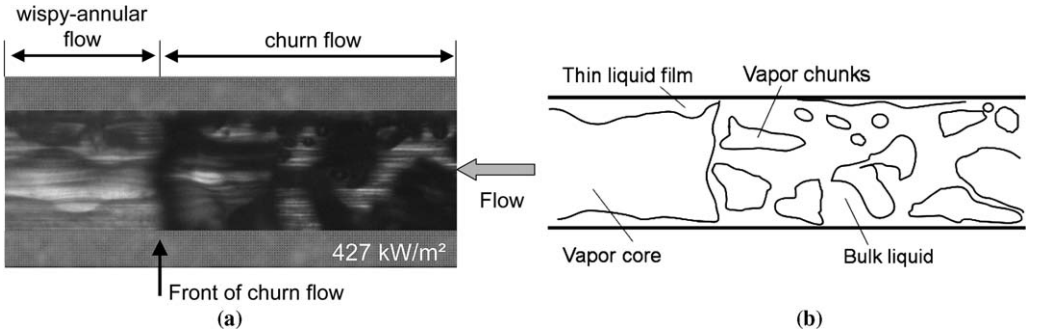

Fig. 7. (a) Visualization of commencement of churn flow following wispy-annular flow at the heat flux of 427 kW/m^2, and (b) sketch of the visualized pattern.

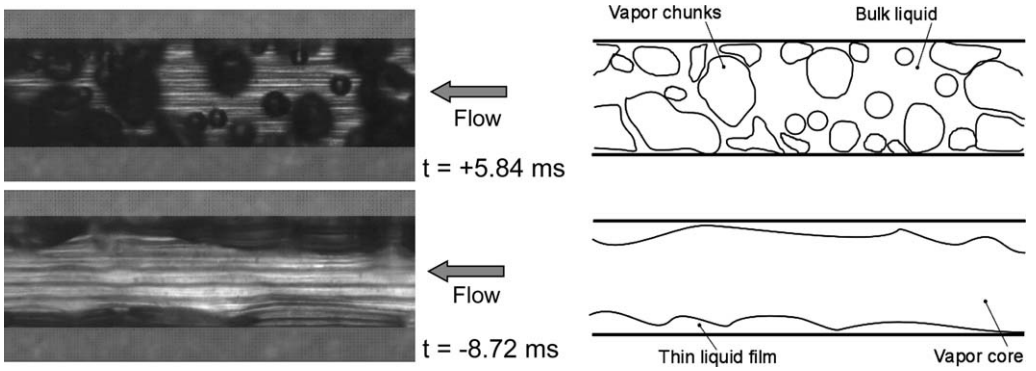

Fig. 8. Churn flow observed 5.84 ms after, and wispy-annular flow observed 8.72 ms before, commencement of churn flow at the instant shown in Fig. 7.

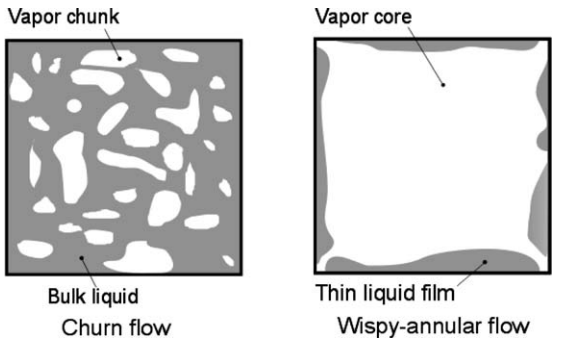

Fig. 9. Channel cross-sections showing sketches of vapor chunks in churn flow and thin liquid films on the channel walls in wispy-annular flow.

Fig. 10 shows a qualitative sketch of the timeframe of the alternating flow patterns. At the reference time of $t = 0$, wispy-annular flow is replaced by churn flow, accompanied with a step decrease in vapor quality. In contrast, the vapor quality gradually increases as the churn flow develops into a wispy-annular pattern.

In order to better understand the reasons for the observed alternating nature of the flow patterns, flow visualizations were performed in the upstream region (near the inlet) of the microchannels at a heat flux at which the alternating flow patterns were observed. The visualizations reveal that the flow in the upstream region pulses in and out of the microchannels and exhibits strong flow reversal at this heat flux. The frequency of

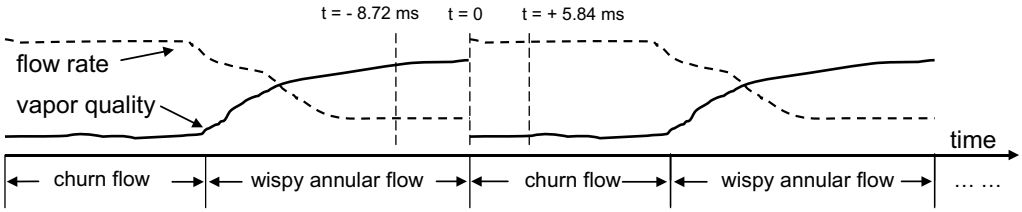

Fig. 10. Schematic illustration of the flow pattern periodicity as a function of time at a heat flux of 427 kW/m^2.

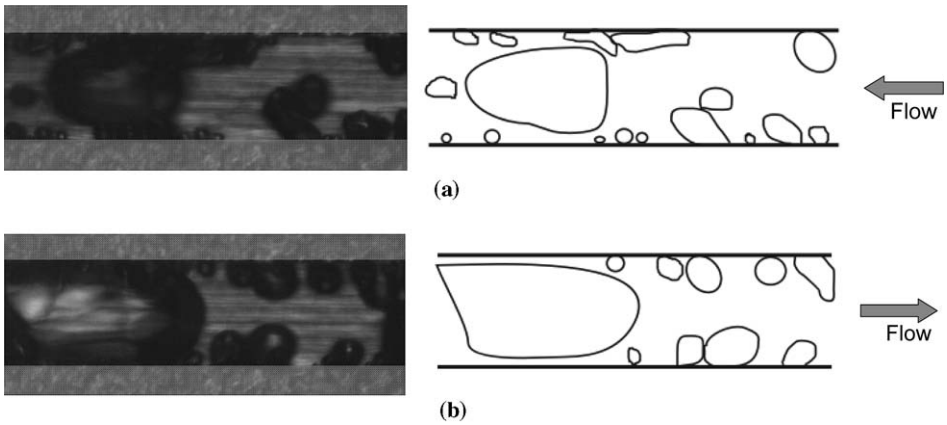

Fig. 11. Flow visualization near the inlet of the microchannels showing transient flow reversal: (a) flow in the direction of flow in the test loop, and (b) flow opposite to the overall direction of flow in the test loop at a different instant.

the pulsation is observed to be approximately 30 Hz, which is the same as the frequency at which wispy-annular and churn flow alternate near the exit of the microchannels. Fig. 11 shows two images captured at two instances when the fluid flows in opposite directions at the microchannel inlet; the image in Fig. 11(b) shows flow in a direction opposite to the flow in the test loop. The flow reversal is apparent from the shapes of the vapor slugs. When flow reverses at a microchannel inlet, it is expected that there is a sudden transient reduction in the flow rate near the channel exit. Since the heat flux is maintained constant, the vapor quality increases during the period of the flow reversal resulting in transition of low-vapor-quality churn flow to high-vapor-quality wispy-annular flow.

A direct consequence of the flow reversal is an increase in fluctuations in the measured pressure drop across the microchannels. Fig. 12 shows the pressure drop time traces at two heat fluxes, the lower of the two being below the level at which flow reversal was observed. It is apparent that the fluctuation strength is significantly increased at the heat flux of 427 kW/m^2 due to the occurrence of flow reversal. The fluctuation strength, quantified as the standard deviation of pressure drop measurements, is seen to increase by approximately 250% once flow reversal is initiated.

4.3. Flow patterns at higher heat fluxes

The alternating wispy-annular and churn flows continue as heat flux is further increased. The patterns in Fig. 13 are captured at heat fluxes of 536 and 617 kW/m^2. At each heat flux, the image at $t = 0$ shows the commencement of churn flow following wispy-annular flow, while the second image shows the flow pattern after a few milliseconds (4.64 and 4.32 ms, respectively for the two heat fluxes). The void fractions during the churn flow at these higher heat fluxes are seen to be much higher than those seen earlier for the lower heat fluxes in Fig. 8. At the heat flux of 536 kW/m^2, as at lower fluxes, the flow pattern in churn flow is characterized by vapor chunks flowing in bulk liquid. As heat flux is increased further, however, the bulk liquid and vapor chunks in churn flow are barely discernible. For heat fluxes greater than 617 kW/m^2, churn flow is

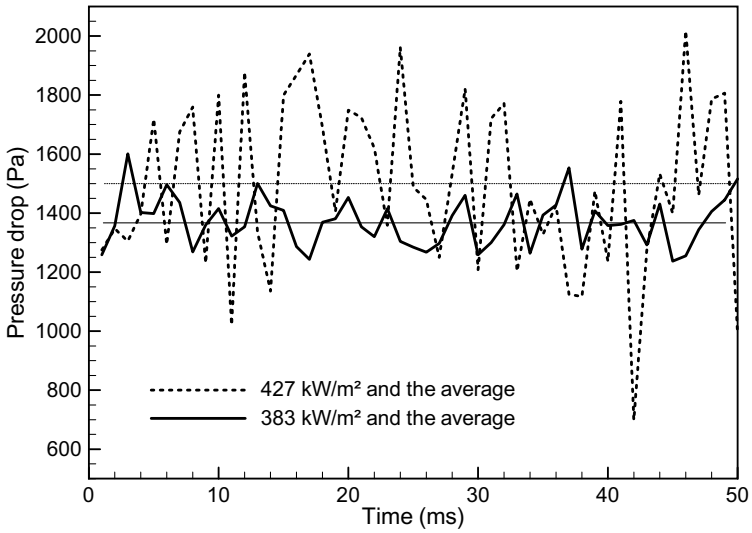

Fig. 12. Pressure drop measurements showing an increase in fluctuations when flow reversal occurs at the inlet of the microchannels at a heat flux of 427 kW/m^2.

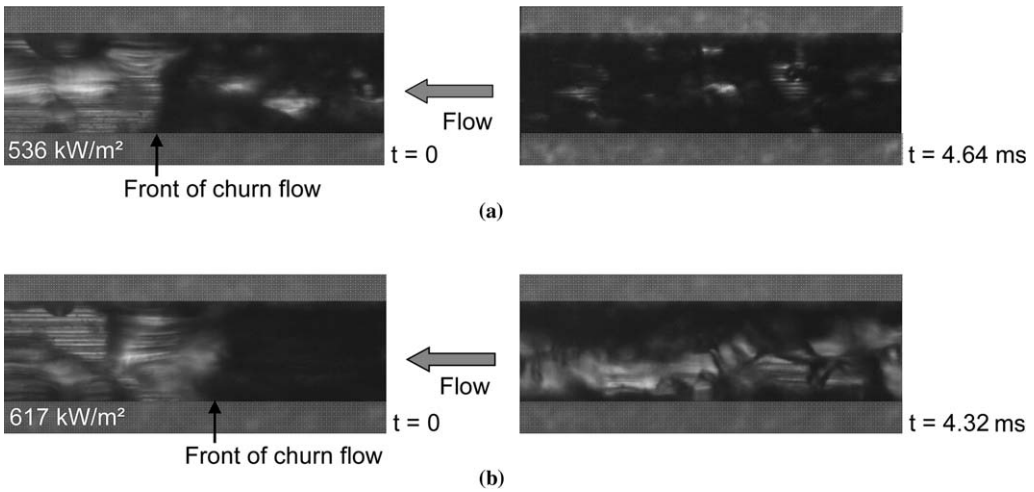

Fig. 13. Images showing the commencement of churn flow (left) at higher heat fluxes of (a) 536 kW/m^2 and (b) 617 kW/m^2, and the flow pattern during the churn flow (right) at the two heat fluxes.

characterized by dispersed liquid (not vapor) chunks flowing in a vapor flow field. These features are shown in the schematic sketches in Fig. 14 which are based on careful observation of the corresponding video clips.[2] Further, the churn flow transitions to a wispy-annular pattern so quickly that the latter period of wispy-annular flow could be severely depleted of liquid resulting in extended partial wall dryout. The wall temperature time traces at various heat fluxes in Fig. 15 show that at heat fluxes of 617 kW/m^2 and higher, the wall temperature exhibits a larger degree of fluctuations. The extended partial wall dryout is responsible for the decrease in the measured heat transfer coefficient with increasing heat flux at heat fluxes 617 kW/m^2 and higher, as was shown earlier in Fig. 5. Fig. 5 also shows that the vapor quality at the point when the heat transfer coefficient starts to decrease is approximately 0.53 for the flow rate of 47 ml/min.

[2] www.ecn.purdue.edu/ECL.

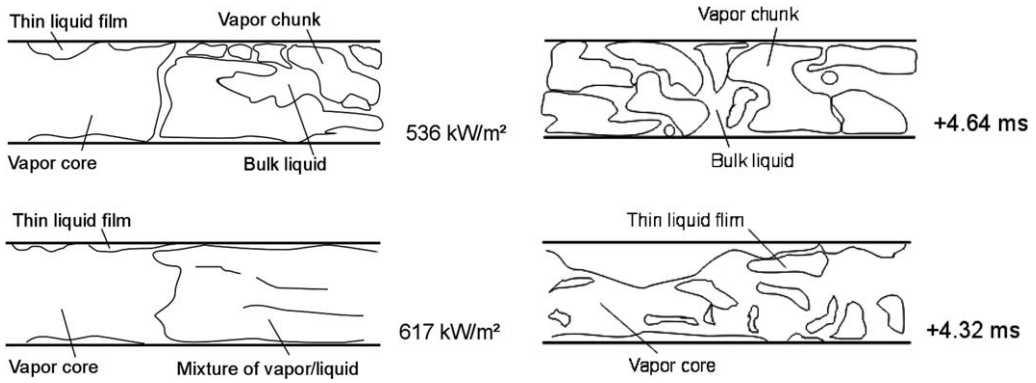

Fig. 14. Schematic drawings of the flow patterns seen in the photographs of Fig. 13.

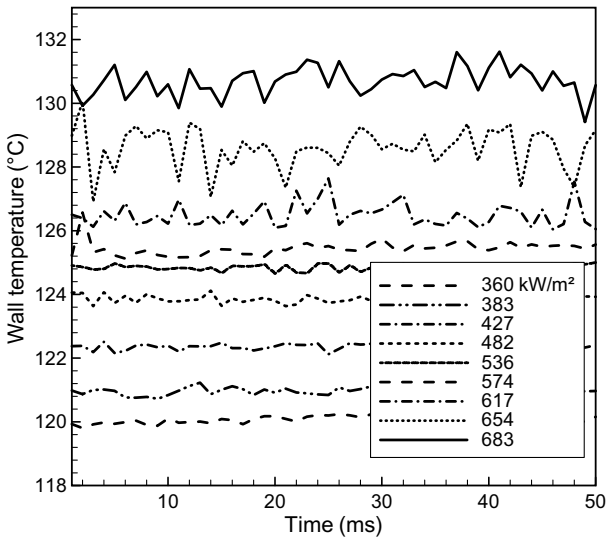

Fig. 15. Time traces of the measured wall temperatures at various heat fluxes.

4.4. Measurements at different flow rates

The heat transfer coefficients and pressure drops measured at three different flow rates of 35, 47 and 60 ml/min are presented in Fig. 16. It is seen in Fig. 16(a) that the heat transfer coefficients for different flow rates exhibit similar behavior with increasing heat flux; they increase with increasing heat flux as fully developed boiling is established, and decrease as extended partial wall dryout occurs at the higher heat fluxes as discussed above for the flow rate 47 ml/min. It may be noted that fully developed boiling is established for heat fluxes of 232, 269 and 310 kW/m^2, respectively, for flow rates of 35, 47 and 60 ml/min. At a higher flow rate, both partial wall dryout and the associated decrease in heat transfer coefficient occur at higher heat fluxes. Before this point of partial dryout is reached, however, the heat transfer coefficients for the different flow rates are largely independent of flow rate over the range considered.

The increase in heat transfer coefficient with increasing heat flux as well as the independence of flow rate are two characteristics of nucleate boiling heat transfer. It is thus appropriate to compare the measurements with predictions from nucleate boiling heat transfer correlations. The Cooper correlation (Cooper, 1984) is selected for this comparison since it has been recommended as one of the more accurate ones for nucleate boiling heat transfer (Collier and Thome, 1994), although it was not proposed for microchannels:

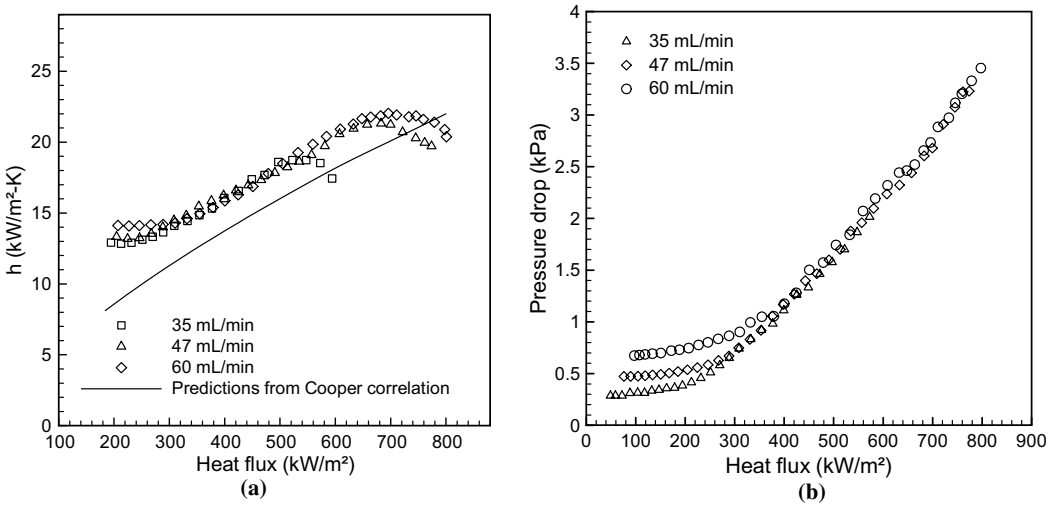

Fig. 16. Heat transfer coefficients and pressure drops measured at three different flow rates. Predicted heat transfer coefficients from the nucleate boiling correlation (Cooper, 1984) are also included.

$$h = 55\, P_r^{0.12}(-\log_{10}P_r)^{-0.55}M^{-0.5}(q'')^{0.67}. \tag{5}$$

In Eq. (5), P_r is the reduced pressure (ratio of the fluid pressure corresponding to the center of the heating element U3 and the critical pressure of FC-77) and M is the molecular weight of FC-77. Since the Cooper correlation was proposed for nucleate boiling heat transfer, the heat flux, q'', in Eq. (5) should be based on the effective wetted area of the microchannels

$$q'' = \frac{\dot{q}_{\text{fluid}}}{A\alpha}, \tag{6}$$

in which $\alpha = (2\eta H + W_c)/(W_c + W_f)$, η is the fin efficiency, H is the channel depth, and W_c and W_f are the channel and fin widths, respectively. The fin efficiency η for rectangular fins is calculated using the average measured heat transfer coefficient based on the wetted area of the microchannels, and varies from 0.92 to 0.95 in this work.

In order to compare with the measurements, the predictions from Eq. (5) are scaled to the heating element area and are included in Fig. 16(a). It is seen that the predictions match the trend of measured heat transfer coefficients, but are lower by 7–42% depending on the heat flux; the larger percentage deviations occur at the lower heat fluxes. The lower heat transfer coefficients predicted by the Cooper correlation could be in part due to the contribution of convective heat transfer, which is larger at lower heat fluxes, and in part since the correlation was proposed for a different, pool boiling situation.

It is seen in Fig. 16(b) that as fully developed boiling is attained in microchannels, the pressure drop for all flow rates increases almost linearly with increasing heat flux and is not affected by the flow reversal and partial wall dryout discussed above. It is interesting to note that the measured pressure drop is also independent of flow rate in this region. Since the liquid at the inlet is moderately subcooled (26 °C subcooling for all flow rates), it is possible that the lack of dependence on flow rate may be due to a balance between friction and acceleration of flow due to phase change. At a given heat flux, a higher flow rate is characterized by a lower vapor quality, which would lead to a larger frictional pressure drop but with a smaller contribution to pressure drop from fluid acceleration. The converse is true for lower flow rates.

5. Summary and conclusions

Flow boiling heat transfer to a dielectric fluid in a microchannel heat sink has been investigated. High-speed visualizations of two-phase flow patterns were obtained at the rate of 12,500 frames per second along with

simultaneous measurements of heat transfer and pressure drop. Four different flow patterns – bubbly flow, slug flow, churn flow and wispy-annular – were observed. The major findings from this work are summarized as follows:

1. Bubbly flow is the dominant flow regime at low heat fluxes and vapor slugs form as a result of bubble coalescence as the heat flux is increased. Heat fluxes at which fully developed boiling is achieved are 232, 269, and 310 kW/m^2, respectively, for the three flow rates of 35, 47, and 60 mL/min.
2. As heat flux is further increased, wispy-annular and churn flow are observed to alternate once flow reversal commences upstream at the microchannel inlet. The flow reversal is reflected as stronger fluctuations in the pressure drop.
3. The vapor quality increases gradually as churn flow develops into wispy-annular flow, while there is a step decrease in vapor quality as churn flow resumes.
4. The flow reversal near the microchannel inlet causes abrupt changes in flow rate near the exit of the microchannels. Given an unchanged heat flux, the change in flow rate is responsible for the alternating flow patterns observed in the downstream of microchannels.
5. As heat flux is further increased (beyond 542, 673, and 730 kW/m^2, respectively, for the three increasing flow rates), heat transfer coefficients decrease with increasing heat flux due to the partial wall dryout. When wall dryout occurs, the fluctuations of wall temperature become stronger.
6. The heat transfer coefficients predicted by the Cooper correlation for nucleate boiling show moderate agreement with the experimental measurements, differing by 7–42% depending on the heat flux; the larger percentage deviations occur at the lower heat fluxes.
7. As fully developed boiling is established in microchannels, time-averaged pressure drop increases with increasing heat flux and is independent of flow rate. The flow instability is not seen to affect the time-averaged pressure drop in the microchannels.

Acknowledgements

Support for this work from the Indiana 21st Century Research and Technology Fund is gratefully acknowledged. The authors would like to thank Bruce Myers, Darrel Peugh, and Suresh Chengalva of Delphi Electronics and Safety, Kokomo, Indiana, for providing the test vehicles for this study and for useful discussions. Ben Jones, Dong Liu and Poh-Seng Lee helped in setting up the high-speed imaging system used in this work.

References

3M Corporation, 1995. 3M Fluorinerts Liquids Product Manual.

Brutin, D., Tadrist, L., 2003. Measurement and prediction of pressure drop in two-phase microchannel heat sinks. Int. J. Heat and Mass Transfer 46, 2737–2753.

Chen, T., Garimella, S.V., 2005. Flow boiling heat transfer to a dielectric coolant in a microchannel heat sink. In: Proceedings of the ASME/Pacific Rim Technical Conference and Exhibition on Integration and Packaging of Micro, Nano, and Electronic Systems (InterPACK '05), San Francisco, July 17–22.

Chen, T., Garimella, S.V., in press. Effects of dissolved air on subcooled flow boiling of a dielectric coolant in a microchannel heat sink. ASME J. Electron. Packag.

Coleman, J.W., Garimella, S., 1999. Characterization of two-phase flow patterns in small diameter round and rectangular tubes. Int. J. Heat and Mass Transfer 42, 2867–2881.

Collier, J.G., Thome, J.R., 1994. Convective Boiling and Condensation, third ed. McGraw Hill, New York.

Cooper, M.G., 1984. Saturated nucleate pool boiling – a simple correlation. In: Proceedings of First UK National Heat Transfer Conference, IChemE Symp. Series No. 86, pp. 785–793.

Hetsroni, G., Mosyak, A., Segal, Z., 2001. Non-uniform temperature distribution in electronic devices cooled by flow in parallel microchannels. IEEE Trans. Components Packag. Technol. 24, 16–23.

Hetsroni, G., Mosyak, A., Segal, Z., Ziskind, G., 2002. A uniform temperature heat sink for cooling of electronic devices. Int. J. Heat and Mass Transfer 45, 3275–3286.

Huo, X., Chen, L., Tian, Y.S., Karayiannis, T.G., 2004. Flowing boiling and flow regimes in small diameter tubes. Appl. Thermal Eng. 24, 1225–1239.

Kandlikar, S.G., 2002. Two-phase flow patterns, pressure drop, and heat transfer during boiling in microchannel flow passages of compact evaporators. Heat Transfer Eng. 23, 5–23.

Kandlikar, S.G., Steinke, M.E., Tian, S., Campbell, L.A., 2001. High-speed photographic observation of flow boiling of water in parallel minichannels. In: Proceedings of 35th National Heat Transfer Conference, Anaheim, CA, June 10–12.

Kew, P.A., Cornwell, K., 1997. Correlations for the prediction of boiling heat transfer in small-diameter channels. Appl. Thermal Eng. 17, 705–715.

Kline, S.J., McClintock, F.A., 1953. Describing uncertainties in single-sample experiments. Mech. Eng. 75, 3–8.

Lazarek, G.M., Black, S.H., 1982. Evaporative heat transfer, pressure drop and critical heat flux in a small diameter vertical tube with R-113. Int. J. Heat and Mass Transfer 25, 945–960.

Lin, L., Udell, K.S., Pisano, A.P., 1994. Phase change phenomena on a heated polysilicon micro heater in confined and unconfined micro channels. Thermal Sci. Eng. 2, 52–59.

Liu, D., Garimella, S.V., 2005. Flow boiling in a microchannel heat sink. In: Proceedings of ASME International Mechanical Engineering Congress and Exposition, Orlando, FL, November 5–11.

Peng, X., Hu, H., Wang, B., 1998. Boiling nucleation during liquid flow in microchannels. Int. J. Heat and Mass Transfer 41, 101–106.

Saitoh, S., Daiguji, H., Hihara, E., 2005. Effect of tube diameter on boiling heat transfer of R-134a in horizontal small-diameter tubes. Int. J. Heat and Mass Transfer 48, 4973–4984.

Thome, J.R., 2004. Boiling in microchannels: a review of experiment and theory. Int. J. Heat and Fluid Flow 25, 128–139.

Wu, H.Y., Cheng, P., 2003. Visualization and measurements of periodic boiling in silicon microchannels. Int. J. Heat and Mass Transfer 46, 2603–2614.

Wu, H.Y., Cheng, P., 2004. Boiling instability in parallel silicon microchannels at different heat flux. Int. J. Heat and Mass Transfer 47, 3631–3641.

Xu, J., Shen, S., Gan, Y., Li, Y., Zhang, W., Su, Q., 2005. Transient flow pattern based microscale boiling heat transfer mechanisms. J. Micromech. Microeng. 15, 1344–1361.